

Path-integral simulation of graphene monolayers under tensile stress

Carlos P. Herrero and Rafael Ramírez

Instituto de Ciencia de Materiales de Madrid, Consejo Superior de Investigaciones Científicas (CSIC), Campus de Cantoblanco, 28049 Madrid, Spain

(Dated: October 21, 2018)

Finite-temperature properties of graphene monolayers under tensile stress have been studied by path-integral molecular dynamics (PIMD) simulations. This method allows one to consider the quantization of vibrational modes in these crystalline membranes and to analyze the influence of anharmonic effects in the membrane properties. Quantum nuclear effects turn out to be appreciable in structural and thermodynamic properties of graphene at low temperature, and they can even be noticeable at room temperature. Such quantum effects become more relevant as the applied stress is increased, mainly for properties related to out-of-plane atomic vibrations. The relevance of quantum dynamics in the out-of-plane motion depends on the system size, and is enhanced by tensile stress. For applied tensile stresses, we analyze the contribution of the elastic energy to the internal energy of graphene. Results of PIMD simulations are compared with calculations based on a harmonic approximation for the vibrational modes of the graphene lattice. This approximation describes rather well the structural properties of graphene, provided that the frequencies of ZA (flexural) acoustic modes in the transverse direction include a pressure-dependent correction.

PACS numbers: 61.48.Gh, 65.80.Ck, 63.22.Rc

I. INTRODUCTION

In recent years there has been a surge of interest on two-dimensional materials, and graphene in particular, due to their unusual electronic, elastic and thermal properties.^{1–4} In fact, graphene displays high values of thermal conductivity,^{5–7} as well as large in-plane elastic constants.⁸ Its mechanical properties are also important for possible applications, such as cooling of electronic devices.^{9,10}

The structural arrangement for pure defect-free graphene corresponds to a planar honeycomb lattice. At finite temperatures, there appear out-of-plane displacements of the C atoms, and for $T \rightarrow 0$, quantum fluctuations related to zero-point motion give rise to a departure of strict planarity of the graphene sheet.¹¹ In particular, one has low-lying vibrational excitations associated to large-scale ripples perpendicular to the plane.¹² Moreover, a graphene sheet can actually bend and depart from planarity for other reasons, such as the presence of defects and external stresses.^{13,14}

A thin membrane crumples in the presence of a compressive stress. This behavior has been investigated during the last three decades in lipid membranes^{15,16} and polymer films.^{17,18} In graphene, crumpling originates from out-of-plane phonons as well as from static wrinkling, and has been observed in both supported and freestanding samples.^{19,20} Mechanical properties such as stiffness and bending rigidity can be renormalized due to crumpling.^{21–23} For graphene, it has been found that the maximum compressive stress that a freestanding sheet can sustain without crumpling decreases with system size, and has been estimated to be about 0.1 N/m at room temperature in the thermodynamic limit.²⁴

A tensile stress applied in the graphene plane does not affect the planarity of the sheet, but causes appreciable

changes in the elastic properties of the material.²⁵ Thus, it has been observed that the in-plane Young modulus is increased by a factor of three when applying a stress of 1 N/m.²⁴ The bending rigidity κ does also change with the tensile stress, and in fact it decreases but not so critically as the in-plane elastic constants. In this context, it is important to note that the actual area per atom, A , is not readily measurable, and the accessible observable is usually its projection, A_p , onto the mean plane of the membrane ($A_p \leq A$). Thus, one may refer the elastic properties of graphene either to the area A or to A_p , which may behave in very different ways. For example, a negative thermal expansion coefficient is found for graphene when one refers to A_p , but the thermal expansion associated to the area A is positive.^{11,26}

Recent experimental and theoretical work has shown the influence of strain in several characteristics of graphene, such as electronic transport, optical properties, and the formation of moiré patterns.²⁷ Similar properties have been also studied in other two-dimensional materials, as metallic dichalcogenides.²⁸

Equilibrium and dynamical properties of graphene have been studied earlier by using Monte Carlo and molecular dynamics simulations. These simulations were based on *ab-initio*,^{26,29–31} tight-binding,^{32–35} and empirical interatomic potentials.^{12,36–40} In most of these simulations, C atoms were treated as classical particles, which is accurate at relatively high temperatures but is not suitable to study thermodynamic variables at low temperature. The quantum character of the atomic motion can be taken into account by employing path-integral simulations, which allow to consider quantum and thermal fluctuations in many-body systems at finite temperatures.^{41,42} Path-integral simulations of a single graphene sheet have been lately performed to study equilibrium properties of this material.^{11,43} Moreover, nu-

clear quantum effects have been studied by a combination of density-functional theory and a quasi-harmonic approximation for vibrational modes in this crystalline membrane.^{44,45}

In this paper, we employ path-integral molecular dynamics (PIMD) simulations to study structural and vibrational properties of graphene under tensile stress. We consider different sizes for the simulation cell, as finite-size effects are known to be important for some properties of graphene.^{11,40,46} The magnitude of nuclear quantum effects in the graphene properties is assessed by comparing the results of PIMD simulations with data obtained from classical simulations. We find that quantum effects are relevant to describe the temperature and pressure dependence of graphene's real and in-plane areas, as well as to describe the amplitude of the out-of-plane motion, especially at low temperatures. Our data indicate that the relevance of nuclear quantum effects increases as tensile stress is raised. Results of PIMD simulations are compared with data derived from a harmonic approximation for the out-of-plane vibrations. This approximation turns out to be rather accurate, provided that the vibrational frequencies of ZA acoustic modes are conveniently renormalized for different applied stresses.

The paper is organized as follows. In Sec. II, we present the computational method used in the simulations. Structural properties such as in-plane A_p and real area A are given in Sec. III as a function of applied stress. Results for the internal, vibrational, and elastic energy of graphene are discussed in Sec. IV. In Sec. V we study the out-of-plane atomic motion, with emphasis on the competition between classical-like and quantum dynamics. In Sec. VI we summarize the main results.

II. COMPUTATIONAL METHOD

We use the PIMD method to obtain equilibrium properties of graphene under tensile stress. This procedure is based on the Feynman path-integral formulation of statistical mechanics, a nonperturbative technique to study many-body quantum systems at finite temperatures.⁴⁷ The implementation of this formulation for numerical simulations is based on an isomorphism between the quantum system and a fictitious classical system, in which each quantum particle is described by a ring polymer (corresponding to a cyclic quantum path) composed of N_{Tr} (Trotter number) *beads*.⁴⁸ This becomes exact in the limit $N_{\text{Tr}} \rightarrow \infty$. Details on this simulation technique can be found elsewhere.^{41,42,49,50} The dynamics in PIMD is artificial, since it does not correspond to the actual dynamics of the real quantum particles. However, it is useful for sampling the many-body configuration space, yielding accurate results for time-independent equilibrium properties of the actual quantum system.

The Born-Oppenheimer surface for the nuclear dynamics is derived here from an effective empirical potential, developed for carbon-based systems, namely the so-called

LCBOPII.⁵¹ This is a long-range carbon bond order potential, which was previously used to perform classical simulations of diamond,⁵¹ graphite,⁵¹ liquid carbon,⁵² as well as graphene sheets.^{12,40,53} A relevant application of this effective potential was the calculation of the carbon phase diagram including diamond, graphite, and the liquid, and showing its precision by comparison of the predicted diamond-graphite line with experimental results.⁵⁴

The LCBOPII potential has been more recently employed to study graphene, giving a good description of elastic properties such as the Young's modulus.^{53,55} According to previous simulations,^{11,24,38} the original LCBOPII parameterization has been slightly modified to increase the zero-temperature bending constant of graphene from 1.1 eV to a value of 1.49 eV, more consistent with experimental data.⁵⁶ This effective potential was lately used to perform PIMD simulations, allowing to assess the extent of quantum effects in graphene sheets from a comparison with results of classical simulations.¹¹

Other effective interatomic potentials have been employed in recent years to study various properties of graphene. In particular, the AIREBO potential model has been widely used in this field.⁵⁷⁻⁶¹ Comparing the LCBOPII and AIREBO models, we find that they yield very similar equilibrium C-C distance and in-plane thermal expansion coefficient, as derived from classical molecular dynamics simulations.^{11,58,61} Results for the Young's modulus of graphene derived from the LCBOPII potential are closer to those given by *ab initio* calculations.⁵⁸

The calculations presented here were carried out in the isothermal-isobaric ensemble, where we fix the number of carbon atoms (N), the applied stress (P), and the temperature (T). We employed effective algorithms for carrying out PIMD simulations in this statistical ensemble, as those presented in the literature.⁶²⁻⁶⁵ Specifically, we used staging variables to define the bead coordinates, and the constant-temperature ensemble was achieved by coupling chains of four Nosé-Hoover thermostats. A supplementary chain of four barostats was coupled to the area of the simulation box to give the required pressure P .^{50,63} The kinetic energy K has been calculated by using the so-called virial estimator, which has a statistical uncertainty smaller than the potential energy, V , of the system.^{63,66} Other technical details about the simulations presented here are the same as those given elsewhere.⁶⁷⁻⁶⁹

Atomic forces were analytically derived from position derivatives of the instantaneous potential energy U (note that $V = \langle U \rangle$). The estimator of the two-dimensional (2D) stress tensor τ is the same as that employed in previous works,^{24,38} and its formulation for PIMD simulations of graphene is similar to that given earlier for three-dimensional (3D) solids.^{50,70} Details on the pressure estimator employed here are presented in Appendix A. The mechanical stress P in the (x, y) plane of graphene is obtained from the trace of the tensor τ :

$$P = \frac{1}{2} (\tau_{xx} + \tau_{yy}) . \quad (1)$$

Note that in the case of applying a large compressive stress ($P > 0$, not considered here), one may have severe bending or crumpling of the graphene sheet. In this case the in-plane stress P may appreciably differ from the actual stress felt by the *real* graphene surface (related to the area A).^{24,71}

We consider rectangular simulation cells with similar side lengths L_x and L_y in the x and y directions of the reference plane, and periodic boundary conditions were assumed. Sampling of the configuration space has been carried out at temperatures between 12 K and 2000 K. For comparison with results of PIMD simulations, some classical molecular dynamics (MD) simulations have been also performed. In our context this is achieved by setting $N_{\text{Tr}} = 1$. For the quantum simulations, N_{Tr} was taken proportional to the inverse temperature: $N_{\text{Tr}} T = 6000$ K, which roughly gives a constant precision in the PIMD results at different temperatures.^{67–69} Cells of size up to 8400 and 14720 atoms were considered for PIMD and classical MD simulations, respectively. For a given temperature, a typical simulation run consisted of 3×10^5 PIMD steps for system equilibration, followed by 4×10^6 steps for the calculation of ensemble average properties.

III. STRUCTURAL PROPERTIES

The simulations presented here were performed in the isothermal-isobaric ensemble, as explained above in Sec. II. Thus, in a simulation run we fix the number of carbon atoms N , the temperature T , and the applied stress P in the (x, y) plane, allowing for changes in the in-plane area of the simulation cell for which periodic boundary conditions are assumed. Carbon atoms are free to move in the out-of-plane direction (z coordinate), and in general any measure of the *real* surface of a graphene sheet at $T > 0$ should give a value larger than the area of the simulation cell in the (x, y) plane. In this line, there has appeared in recent years a discussion in the context of biological membranes, dealing with the question whether it is more convenient to describe the properties of those membranes using the concept of a real surface rather than a *projected* (in-plane) surface.^{72–74} The same question has been also recently raised for crystalline membranes such as graphene.^{11,24,26,75} This can be important for addressing the calculation of thermodynamic properties, because the in-plane area A_p is the variable conjugate to the stress P used in our simulations, and the real area A (also called effective, true, or actual area in the literature^{71–74}) is conjugate to the usually-called surface tension.¹⁶ The difference $A - A_p$ has been recently denoted as *hidden* area by Nicholl *et al.*⁷⁵

The real area A in 3D space is calculated here by a triangulation based on the atomic positions along a simulation run. A is obtained from the areas associated to $N/2$ structural hexagons. Each hexagon contributes by a sum of six triangles, each one formed by the positions of two neighboring carbon atoms and the barycenter of

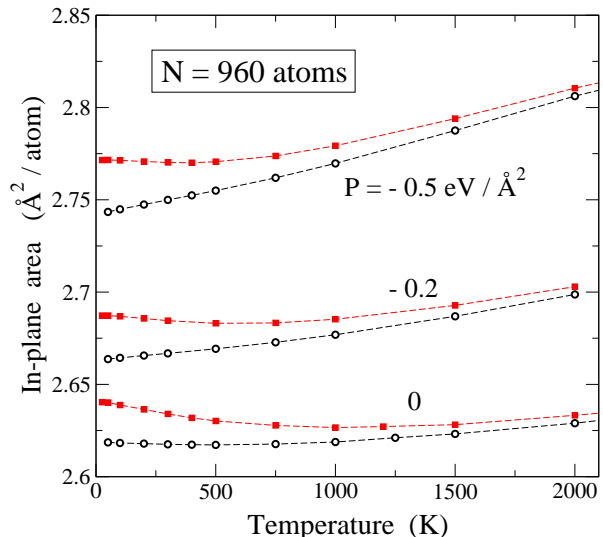


FIG. 1: In-plane area A_p vs. temperature for graphene, as derived from classical (open circles) and PIMD simulations (solid squares) for $N = 960$ and different stresses. From bottom to top: $P = 0, -0.2$, and $-0.5 \text{ eV } \text{Å}^{-2}$. Error bars are less than the symbol size. Lines are guides to the eye.

the hexagon (mean point of its six vertices).²⁴ There are other similar definitions that can be employed for the area A , as those based on the interatomic distance C–C.^{11,76} The area A based on triangulation employed here seems more precise to deal with the 2D nature of a graphene layer in 3D space. It has been shown earlier that A has a very small size effect, in fact negligible in comparison with that appearing for A_p .²⁴

In Fig. 1 we show the temperature dependence of the in-plane area A_p , obtained from classical MD (open circles) and PIMD simulations (solid squares) for a supercell with $N = 960$ atoms. Results are given for $P = 0, -0.2$, and $-0.5 \text{ eV } \text{Å}^{-2}$. Tensile stress causes not only an increase in A_p , but its temperature dependence also changes. For each considered value of the stress, the curve $A_p(T)$ derived from quantum simulations displays a minimum, that shifts to lower temperatures as the tensile stress is increased. Thus, such a minimum evolves from $T_m \approx 1000$ K for $P = 0$ to ≈ 400 K for $P = -0.5 \text{ eV } \text{Å}^{-2}$. In the classical simulations, however, one finds a shallow minimum for $P = 0$, that is absent for the tensile stresses shown in Fig. 1 (in fact we did not observe it for $P = -0.1 \text{ eV } \text{Å}^{-2}$ either, not shown in the figure). The classical results for $P = 0$ are similar to those found in earlier classical Monte Carlo and MD simulations of graphene single layers.^{43,46,53}

At low T the results of PIMD simulations verify $dA_p/dT \rightarrow 0$, i.e., the corresponding curves shown in Fig. 1 (solid symbols) become flat close to $T = 0$, as required by the third law of thermodynamics. In the limit $T \rightarrow 0$, the difference between quantum and classical results converges to $0.022 \text{ Å}^2/\text{atom}$ in the absence of applied stress ($P = 0$). This difference decreases for rising

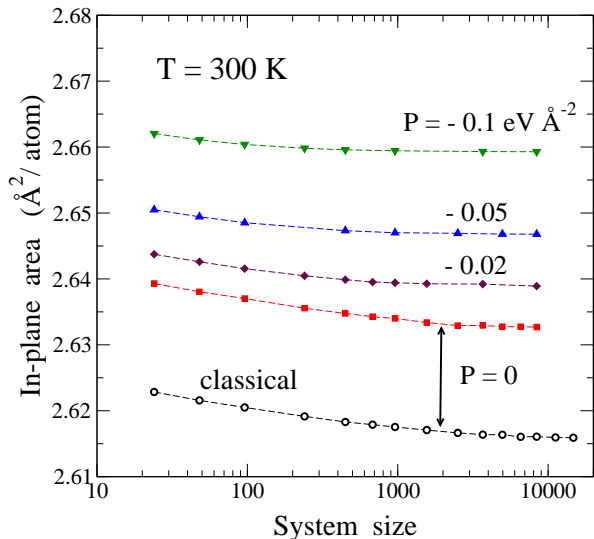


FIG. 2: In-plane area A_p vs. system size, as derived from PIMD simulations for $T = 300$ K and various tensile stresses (solid symbols). From top to bottom: $P = -0.1$ (triangles down), -0.05 (triangles up), -0.02 (diamonds), and 0 eV \AA^{-2} (squares). For comparison, open squares indicate results of classical MD simulations for $P = 0$. Error bars are less than the symbol size. Lines are guides to the eye.

temperature, as nuclear quantum effects become less important. For $P = -0.5$ eV \AA^{-2} , we find for $T \rightarrow 0$ a difference of 0.031 $\text{\AA}^2/\text{atom}$. The increase in A_p at low temperature is due to zero-point motion associated to in-plane acoustic modes (LA and TA). The frequency of these modes decreases for increasing A_p (i.e., when tensile stress is increased, according to positive Grüneisen parameters), and therefore their vibrational amplitudes are larger. This causes a larger zero-point expansion of A_p for larger tensile stress.

The presence of a minimum in the $A_p(T)$ curves derived from PIMD simulations is due to two competing effects, as discussed earlier for graphene without stress.^{11,46,77} On one hand, the area A increases as temperature is raised, and on the other hand, surface bending gives rise to a decrease in its 2D projection, i.e., A_p . At low T , this decrease associated to out-of-plane motion dominates the thermal expansion of the real surface, and $dA_p/dT < 0$. For the quantum results, the thermal expansion at low T is very small compared to the classical calculations for which $\lim_{T \rightarrow 0} dA/dT > 0$, thus causing a more appreciable decrease in A_p for raising T in the quantum case. At high temperatures, the increase in A predominates over the contraction in the projected area due to out-of-plane motion.

For unstressed graphene it has been indicated that finite-size effects can be important for several structural properties of the crystalline membrane.^{11,24} It is now worthwhile to consider finite-size effects for the in-plane area of graphene under stress. In Fig. 2 we present the size dependence of A_p for several tensile stresses. In all

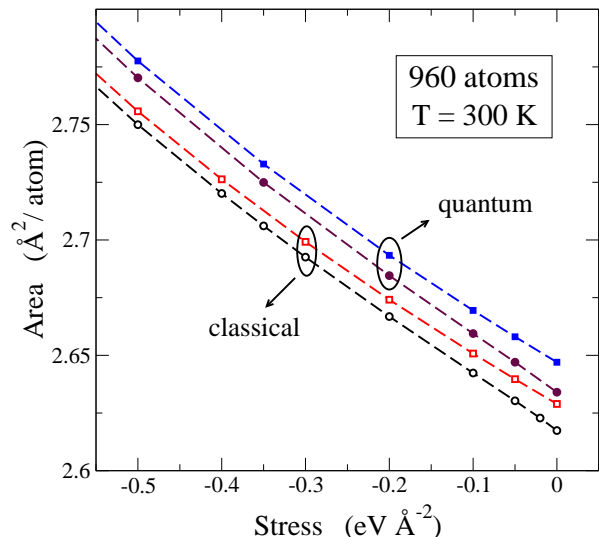


FIG. 3: Real area A and in-plane area A_p of graphene vs. tensile stress, as derived from classical (open symbols) and PIMD simulations (solid symbols) for $N = 960$ and $T = 300$ K. Squares and circles correspond to A and A_p , respectively. Error bars are less than the symbol size. Lines are guides to the eye.

cases, A_p decreases for increasing N , and reaches a well-defined plateau for large sizes. One observes that the convergence to the large-size value is faster for larger tensile stress. Moreover, the difference between the large-size limit and the value corresponding to $N = 24$ (the smallest supercell considered here) appreciably decreases from 6.7×10^{-3} $\text{\AA}^2/\text{atom}$ for $P = 0$ to 2.8×10^{-3} $\text{\AA}^2/\text{atom}$ for $P = -0.1$ eV \AA^{-2} .

For comparison, we also present in Fig. 2 results for $A_p(N)$ derived from classical MD simulations at 300 K. The difference between quantum and classical results for $P = 0$ amounts to 0.017 $\text{\AA}^2/\text{atom}$, and it is nearly constant for the system sizes considered here. This difference increases to 0.022 $\text{\AA}^2/\text{atom}$ at $P = 0$ in the low-temperature limit, as indicated above (see Fig. 1). For $P = -0.1$ eV \AA^{-2} and $T = 300$ K, our classical simulations yield an $A_p(N)$ curve similar to the quantum one (not shown in Fig. 2 to avoid overcrowding). In particular, for a system size $N = 960$, we found an in-plane area $A_p = 2.6423$ $\text{\AA}^2/\text{atom}$, so that the difference between classical and quantum results at this tensile stress is similar to that found for $P = 0$. It is interesting to note that the increase in area A_p due to quantum nuclear motion at 300 K is the same as that caused by a relatively large tensile stress of about -0.07 eV \AA^{-2} (~ -1 N/m).

We now turn to the real surface of graphene and its measure through the area A . It was shown earlier from simulations at $P = 0$ that the surface A is larger than A_p , and the difference between both increases with temperature. This is clear from the fact that A_p is a 2D projection of A , and the actual surface becomes increasingly bent as temperature is raised and the amplitude of out-of-plane

atomic vibrations becomes larger. An important difference between the temperature dependence of A and A_p is that the latter first decreases for increasing T and then it increases at higher T , with a minimum at a temperature T_m . For rising tensile stress, the vibrational amplitude in the z direction decreases (see below), so that the temperature T_m of minimum A_p is lowered. This becomes even clearer in the results of classical simulations, for which the shallow minimum in the curve $A_p(T)$ disappears at relatively low pressures, and it is not observed in the data presented for $P = -0.2$ and -0.5 eV \AA^{-2} in Fig. 1. For the area A one does not observe the decrease displayed by A_p in both classical and quantum simulations at low temperatures (see Ref. 11 for results at $P = 0$).

In Fig. 3 we present the areas A and A_p vs. tensile stress for a simulation cell including 960 atoms. In both cases, we present results from classical (open symbols) and PIMD (solid symbols) simulations. Circles correspond to the in-plane area A_p , whereas squares represent data for the real area A . One notices that quantum effects are appreciable at room temperature. The main aspects of this figure are the following. Tensile stress causes an increase of about 5% in both A and A_p from $P = 0$ to -0.5 eV \AA^{-2} . Moreover, quantum nuclear effects cause in both cases a surface expansion of about 0.02 $\text{\AA}^2/\text{atom}$, which increases slightly as the tensile stress is raised.

To make connection of our results derived from atomistic simulations with an analytical formulation of crystalline membranes, we note that the relation between A and A_p can be expressed in the continuum limit (macroscopic view) as^{24,72,73}

$$A = \int_{A_p} dx dy \sqrt{1 + (\nabla h(x, y))^2}, \quad (2)$$

where $h(x, y)$ is the height of the membrane surface, i.e. the distance to the reference (x, y) plane. The difference $A - A_p$ can be calculated in a classical approach by Fourier transformation of the r.h.s. of Eq. (2).^{16,24,74} This requires the introduction of a dispersion relation $\omega(\mathbf{k})$ for out-of-plane modes (ZA band), where $\mathbf{k} = (k_x, k_y)$ are 2D wavevectors. The frequency dispersion in this acoustic (flexural) band can be well approximated by the expression $\rho\omega^2 = \sigma k^2 + \kappa k^4$, consistent with an atomic description of graphene³⁸ ($k = |\mathbf{k}|$; ρ , surface mass density; σ , effective stress; κ , bending modulus). The effective stress σ can be written as $\sigma = \sigma_0 - P$, with a term σ_0 that appears at finite temperature even in the absence of an applied stress ($P = 0$) due to out-of-plane motion (at 300 K, $\sigma_0 \approx 6 \times 10^{-3}$ eV \AA^{-2}).³⁸

After Fourier transformation one has for the area per atom:^{16,74}

$$A = A_p + \frac{k_B T}{2N} \sum_{\mathbf{k}} \frac{1}{\sigma + \kappa k^2}. \quad (3)$$

For large N the sum in Eq. (3) can be approximated by

an integral:²⁴

$$A = A_p \left(1 + \frac{k_B T}{4\pi} \int_{k_0}^{k_m} dk \frac{k}{\sigma + \kappa k^2} \right). \quad (4)$$

The limits in the integral are the cut-off $k_m = (2\pi/A_p)^{1/2}$ and the size-dependent minimum wavevector $k_0 = 2\pi/L$, with $L = (NA_p)^{1/2}$. The integral in Eq. (4) converges provided that $\sigma > 0$, which is the case here. It allows us to explicitly write the size-dependent ratio A/A_p as

$$\frac{A}{A_p} = \left(\frac{A}{A_p} \right)_{\infty} - \frac{k_B T}{8\pi\kappa} \ln \left(1 + \frac{4\pi^2\kappa}{NA_p\sigma} \right) \quad (5)$$

with the large-size limit ($N \rightarrow \infty$ or $k_0 \rightarrow 0$):

$$\left(\frac{A}{A_p} \right)_{\infty} = 1 + \frac{k_B T}{8\pi\kappa} \ln \left(1 + \frac{2\pi\kappa}{\sigma A_p} \right). \quad (6)$$

Eq. (5), although in principle not very accurate for small system size, yields for $N = 24$, $P = 0$, and $T = 300$ K ($\sigma = 6 \times 10^{-3}$ eV \AA^{-2} , $\kappa = 1.7$ eV; see Ref. 24) a shift in A/A_p of -3.1×10^{-3} , which translates into an increase in A_p of 8.1×10^{-3} $\text{\AA}^2/\text{atom}$ with respect to the large-size limit. From the results of our simulations we find a size effect in A_p of 7.0×10^{-3} $\text{\AA}^2/\text{atom}$ for $N = 24$. Note that, apart from the replacement of the sum in Eq. (3) by an integral, the above expressions assume harmonic vibrations for out-of-plane motion, which becomes less accurate as temperature increases for the onset of larger anharmonicity. Note also the appearance of the stress $\sigma (= \sigma_0 - P)$ in the logarithmic term in Eq. (5), which causes that an increase in tensile stress (P more negative) gives rise to a faster convergence of the area A_p with system size, according to the results shown in Fig. 2.

IV. INTERNAL ENERGY

At $T = 0$ and zero applied stress we find with the LCBOP II potential in a classical approach a strictly planar graphene surface with an interatomic distance $d_{C-C} = 1.4199$ \AA , i.e., an area of 2.6189 \AA^2 per atom, which we call A_0 . This corresponds to a graphene sheet with fixed atomic nuclei on their equilibrium sites without spatial delocalization, giving the minimum energy E_0 , taken as a reference for our calculations at nonzero temperature and applied stress. In a quantum approach, the limit $T \rightarrow 0$ includes out-of-plane atomic fluctuations associated to zero-point motion, and the graphene sheet is not strictly planar. In addition, anharmonicity of in-plane vibrations gives rise to a zero-point lattice expansion (increase in the area A , see Sec. III), which for $T \rightarrow 0$ yields an interatomic distance $d_{C-C} = 1.4287$ \AA , around 1% larger than the classical minimum.

The internal energy E is calculated as a sum of the kinetic K and potential energy V obtained from the simulations at a given temperature. In our simulations of

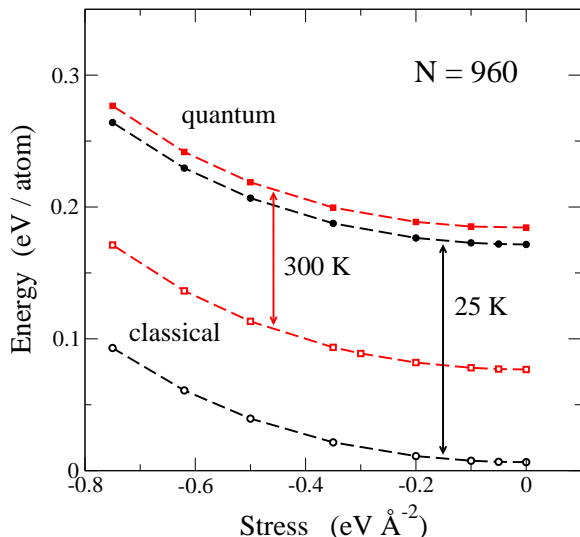


FIG. 4: Dependence of the internal energy of graphene on tensile stress, as derived from classical (open symbols) and PIMD simulations (solid symbols) at two temperatures: 25 K (circles) and 300 K (squares). These results were obtained for a simulation cell including 960 carbon atoms. Vertical arrows indicate the increase in internal energy due to quantization of nuclear motion at each temperature. Error bars are less than the symbol size.

graphene, K and V have been found to slightly increase with system size, and their convergence is rather fast. Thus, for cells in the order of 200 atoms the size effect in the internal energy is almost inappreciable when compared to the largest cells.¹¹ The kinetic energy is associated to vibrational motion of carbon atoms (in-plane and out-of-plane), but the potential energy includes contributions due to atomic vibrations and to the elastic energy due to changes in the area A of graphene at finite temperatures and applied stresses (see below).

In Fig. 4 we display the stress dependence of the internal energy, $E - E_0$, as derived from classical and PIMD simulations for system size $N = 960$. Results are shown for $T = 25$ K (circles) and 300 K (squares). Open and solid symbols correspond to classical and PIMD simulations, respectively. At $P = 0$, the classical energy per atom is basically given by the vibrational energy $E_{\text{vib}}^{\text{cl}} = 3k_B T$, as follows from the equipartition theorem in a harmonic approximation (HA). As the tensile stress is increased (P more negative), the classical internal energy increases for a given temperature, due to the contribution of the elastic energy associated to a finite strain in the graphene lattice. The behavior of the quantum results shown in Fig. 4 is similar to the classical ones. The main difference is the increase in internal energy caused by quantization of the nuclear motion. For zero stress, this increase amounts to 165 meV/atom at 25 K and 107 meV/atom at 300 K. These shifts do not appreciably change in the stress region considered here, and in fact the difference between quantum and classical

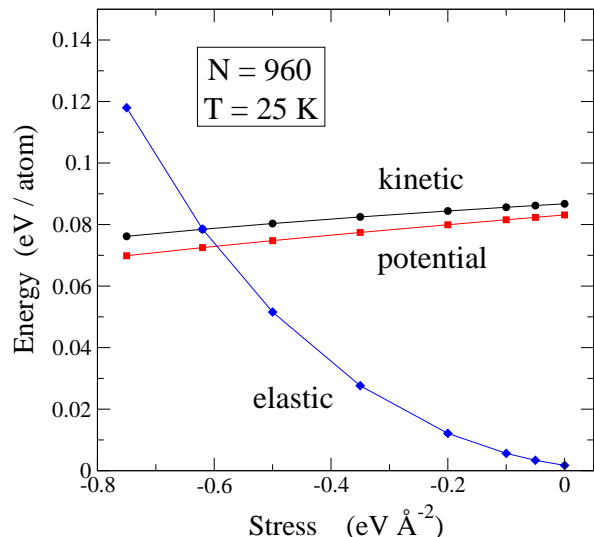


FIG. 5: Different contributions to the internal energy of graphene, as functions of tensile stress. Symbols indicate results of PIMD simulations for $N = 960$ atoms and $T = 25$ K. Diamonds, elastic energy; circles, kinetic energy; squares, vibrational potential energy. Error bars are less than the symbol size. Lines are guides to the eye.

results appears to be nearly constant in the results shown in Fig. 4.

To analyze the different contributions to the internal energy, $E(T)$, we write

$$E(T) = E_0 + E_{\text{el}}(A) + E_{\text{vib}}(A, T). \quad (7)$$

In this expression $E_{\text{el}}(A)$ is the elastic energy corresponding to an area A , and $E_{\text{vib}}(A, T)$ is the vibrational energy of the system. Although not explicitly indicated, the area A is a function of the stress P and temperature T . Our simulations give $E(T)$, and using Eq. (7) we can then split the internal energy $E(T) - E_0$ into an elastic and a vibrational part. The vibrational contribution E_{vib} can in turn be split into kinetic and potential energy parts: $E_{\text{vib}} = V_{\text{vib}} + K$.

The elastic energy $E_{\text{el}}(A)$ is defined here as the increase in energy corresponding to a strictly planar graphene layer with area A respect to the minimum energy E_0 . Thus, we have calculated $E_{\text{el}}(A)$ for a supercell including 960 carbon atoms, expanding it isotropically and keeping it flat. Finite-size effects on the elastic energy are very small, and in fact negligible for our current purposes, as happens for the size dependence of the area A . For $A > A_0$, the elastic energy increases with A , and for small lattice expansion it can be approximated as $E_{\text{el}}(A) \approx C(A - A_0)^2$, with $C = 2.41 \text{ eV } \text{\AA}^{-2}$. At room temperature ($T \sim 300$ K) and for small stresses P (A close to A_0), the elastic energy is much smaller than the vibrational energy E_{vib} , but this can be different for low T and/or large applied stresses (see below). Once calculated the elastic energy for the area A resulting from the simulations at given T and P , we obtain the vibrational

energy $E_{\text{vib}}(A, T)$ by subtracting the elastic energy from the internal energy $E(T)$: $E_{\text{vib}} = E(T) - E_0 - E_{\text{el}}(A)$ (see Eq. (7)). Then, the potential energy corresponding to vibrational motion, V_{vib} , is found as $V_{\text{vib}} = E_{\text{vib}} - K$.

In Fig. 5 we present the different contributions to the internal energy of graphene vs. tensile stress, as derived from PIMD simulations for $N = 960$ atoms and $T = 25$ K. In this figure, diamonds represent the elastic energy, and circles and squares indicate K and V_{vib} , respectively. At $P = 0$, E_{el} is close to zero, but slightly positive, as a consequence of the zero-point expansion of the graphene lattice, which causes that $A > A_0$. For increasing tensile stress, E_{el} rises and becomes similar to K and V_{vib} for $P \approx -0.6$ eV \AA^{-2} . At still larger tensile stress, the elastic contribution is the largest one, as shown in Fig. 5. For $T = 300$ K the picture is qualitatively the same. The elastic energy increases roughly a constant value (26 meV/atom) with respect to the results at 25 K in the whole stress range shown in Fig. 5. The same happens for the kinetic energy, with a rise of 6 meV/atom. As a result, the crossing of E_{el} and K at 300 K occurs for a tensile stress $P \approx -0.55$ eV \AA^{-2} .

For a purely harmonic model for the vibrational modes, one expects $K = V_{\text{vib}}$ (virial theorem^{47,78}), i.e., an energy ratio $K/V_{\text{vib}} = 1$ at any temperature in both classical and quantum approaches. This is not strictly the case for the results of our PIMD, because the vibrational amplitudes are finite, even at low temperatures, and feel the anharmonicity of the interatomic potential. In particular, we find $K > V_{\text{vib}}$, for all temperatures and tensile stresses considered here. As displayed in Fig. 5 for $T = 25$ K, the difference $K - V_{\text{vib}}$ increases as the tensile stress is raised, so that K is about 5% larger than V_{vib} for small stress, and around 9% larger for a stress of -0.75 eV \AA^{-2} . Differences between the kinetic and potential contribution to the vibrational energy have been used for a quantification of the anharmonicity in condensed matter, as discussed earlier from path-integral simulations, e.g., for van der Waals solids⁷⁹ and H impurities in silicon.⁸⁰

Concerning the energy results for our quantum approach at low T , we note that analyses of anharmonicity in solids, based on quasiharmonic approximations and perturbation theory indicate that low-temperature changes in the vibrational energy with respect to a harmonic calculation are mostly due to the kinetic energy. Thus, considering perturbed harmonic oscillators with perturbations of type x^3 or x^4 at $T = 0$, first-order changes in the energy are due to changes in K , and the potential energy stays unshifted in its unperturbed value.^{80,81}

V. OUT-OF-PLANE MOTION

In this section we study the mean-square displacements of carbon atoms in the z direction, normal to the graphene sheet, as obtained from our PIMD simulations. We mostly concentrate on the nature of these atomic

displacements, i.e., if they can be well described by a classical model, or the C atoms appreciably behave as quantum particles. We expect of course that a classical description will lose accuracy as the temperature is reduced, but in the case of graphene it has been shown earlier that other factors such as the system size play also an important role in this question.¹¹ Moreover, an external stress modifies the vibrational frequencies in the material, thus causing a change in the vibrational amplitudes and in the accuracy of a classical description at a given temperature.

PIMD simulations can be used to study vibrational amplitudes or atomic delocalization at finite temperatures. This includes a thermal (classical-like) motion, as well as a delocalization due to the quantum nature of the atomic nuclei, which can be quantified by the spacial extension of the paths associated to a given atomic nucleus. For each quantum path, we define the center-of-gravity (centroid) as

$$\bar{\mathbf{r}}_i = \frac{1}{N_{\text{Tr}}} \sum_{j=1}^{N_{\text{Tr}}} \mathbf{r}_{ij}, \quad (8)$$

where $\mathbf{r}_{ij} \equiv (x_{ij}, y_{ij}, z_{ij})$ is the 3D position of bead j in the ring polymer associated to nucleus i . For the out-of-plane motion, we focus on the z -coordinate of the polymer beads. Then, the mean-square displacement $(\Delta z)_i^2$ of the atomic nucleus i in the z direction along a PIMD simulation run is defined as

$$(\Delta z)_i^2 = \frac{1}{N_{\text{Tr}}} \left\langle \sum_{j=1}^{N_{\text{Tr}}} (z_{ij} - \langle \bar{z}_i \rangle)^2 \right\rangle, \quad (9)$$

The kinetic energy of a particle is related to its quantum delocalization, or in the present context, to the spread of the paths associated to it. This can be measured by the mean-square *radius-of-gyration* of the ring polymers, with an out-of-plane component:^{41,82}

$$Q_{z,i}^2 = \frac{1}{N_{\text{Tr}}} \left\langle \sum_{j=1}^{N_{\text{Tr}}} (z_{ij} - \bar{z}_i)^2 \right\rangle. \quad (10)$$

The total spatial delocalization $(\Delta z)_i^2$ of atomic nucleus i in the z direction at a finite temperature includes, in addition to $Q_{z,i}^2$, another contribution which accounts for the classical-like motion of the centroid coordinate \bar{z}_i , i.e.

$$(\Delta z)_i^2 = Q_{z,i}^2 + C_{z,i}^2, \quad (11)$$

with

$$C_{z,i}^2 = \left\langle (\bar{z}_i - \langle \bar{z}_i \rangle)^2 \right\rangle = \langle \bar{z}_i^2 \rangle - \langle \bar{z}_i \rangle^2. \quad (12)$$

This term $C_{z,i}^2$ converges at high T to the mean-square displacement $(\Delta z)_{i,\text{cl}}^2$ given by a classical model, since in this limit each quantum path collapses onto a single point ($Q_{z,i}^2 \rightarrow 0$). In the results presented below, we will

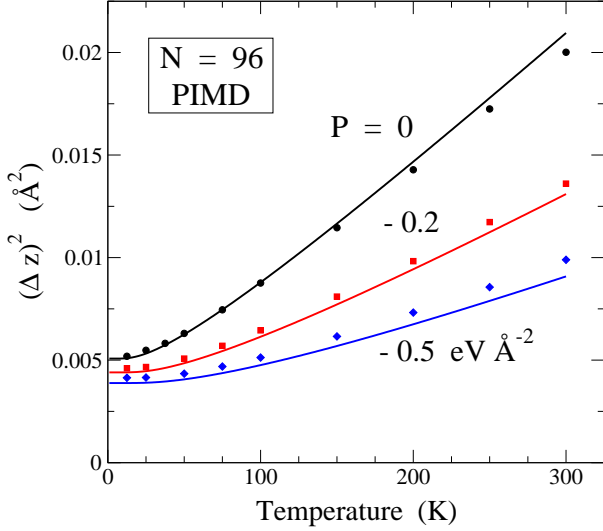


FIG. 6: Mean-square displacement in the z direction as a function of temperature, as derived from PIMD simulations for $N = 96$ and $P = 0$ (circles), -0.2 (squares), and -0.5 eV \AA^{-2} (diamonds). Error bars are in the order of the symbol size. Bold lines correspond to a harmonic approximation based on ZA and ZO vibrational modes.

show data for $(\Delta z)^2$, Q_z^2 , and C_z^2 , calculated as averages for the N atoms in a simulation cell. For example:

$$(\Delta z)^2 = \frac{1}{N} \sum_{i=1}^N (\Delta z)_i^2. \quad (13)$$

To connect the results of our simulations with the out-of-plane displacements corresponding to vibrational modes of the graphene sheet, we recall that the atomic mean-square displacement at temperature T is given in a HA by

$$(\Delta z)_{\text{HA}}^2 = \frac{1}{N} \sum_{i,\mathbf{k}} \frac{\hbar}{2m\omega_i(\mathbf{k})} \coth\left(\frac{\hbar\omega_i(\mathbf{k})}{2k_B T}\right), \quad (14)$$

where the index i ($i = 1, 2$) refers to the phonon bands ZA and ZO, with atomic displacements along the z direction.^{44,83,84} The sum in \mathbf{k} is extended to wavevectors $\mathbf{k} = (k_x, k_y)$ in the hexagonal Brillouin zone, with discrete \mathbf{k} points spaced by $\Delta k_x = 2\pi/L_x$ and $\Delta k_y = 2\pi/L_y$.³⁸ Eq. (14) has been used here to calculate $(\Delta z)_{\text{HA}}^2$ in a harmonic approach. Increasing the system size N causes the appearance of vibrational modes with longer wavelength λ . In fact, one has for the phonons an effective wavelength cut-off $\lambda_{\text{max}} \approx L$, with $L = (NA_p)^{1/2}$, and the minimum wavevector is $k_0 = 2\pi/\lambda_{\text{max}}$, i.e., $k_0 \sim N^{-1/2}$. For the calculations presented below, based on the formula in Eq. (14), we have used the vibrational frequencies in the phonon branches ZA and ZO obtained from diagonalization of the dynamical matrix corresponding to the LCBOPH potential employed here.

For an applied stress P , the most important effect in the ZA and ZO bands is a change in frequency of the ZA

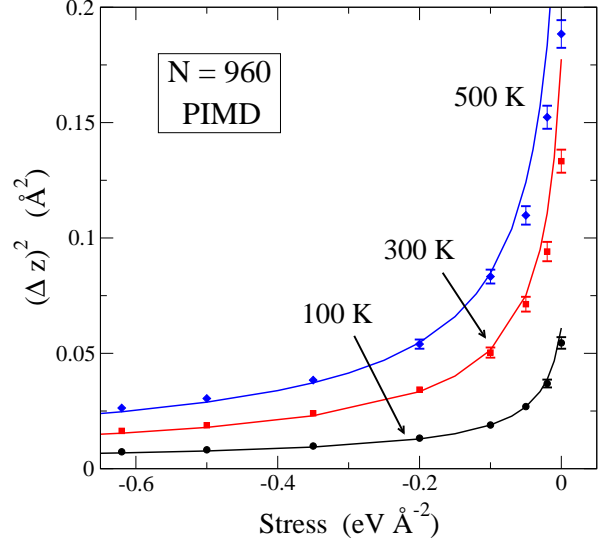


FIG. 7: Mean-square displacement in the z direction as a function of tensile stress, as derived from PIMD simulations for $N = 960$ and three temperatures: $T = 500$ K (diamonds), 300 K (squares), and 100 K (circles). Error bars, when not displayed, are in the order or less than the symbol size. Bold lines correspond to a harmonic approximation based on ZA and ZO vibrational modes.

modes in the low-frequency region, for which

$$\omega_{\text{ZA}}(\mathbf{k})^2 = \omega_{\text{ZA}}^0(\mathbf{k})^2 - \frac{P}{\rho} k^2 \quad (15)$$

The zero-stress band $\omega_{\text{ZA}}^0(\mathbf{k})$ calculated for the minimum-energy structure (area A_0), verifies for small k : $\rho\omega_{\text{ZA}}^0(\mathbf{k})^2 \approx \kappa k^4$. Then, for $P < 0$ the small- k region is dominated by the quadratic term (linear in P) in Eq. (15), so that $\omega_{\text{ZA}}(\mathbf{k}) \approx \sqrt{-P/\rho} k$ for $k \ll 1 \text{ \AA}^{-1}$.

In Fig. 6 we show results for the motion in the out-of-plane direction, obtained for a cell including 96 atoms. The use of a relatively small simulation cell is convenient to visualize the behavior of $(\Delta z)^2$ in the low-temperature region, where quantum effects are prominent. For larger cell sizes, these effects appear only at lower temperatures, which turns out to be difficult to observe from PIMD simulations.¹¹ Solid symbols represent the mean-square displacement $(\Delta z)^2$ derived from the simulations, as a function of temperature for three different applied stresses: $P = 0$ (circles), -0.2 (squares), and -0.5 eV \AA^{-2} (diamonds). Lines were calculated from a harmonic approximation based on the ZA and ZO phonon bands of graphene, as indicated above.

One observes in Fig. 6 that the vibrational amplitude decreases as the tensile stress increases, mainly due to an increase in vibrational frequencies of ZA modes with low k ($k \ll 1 \text{ \AA}^{-1}$). This becomes important as the temperature is raised, but it is also appreciable in the low-temperature region, as shown in the figure. The lines derived from a HA are close to the results of the PIMD simulations at low temperature, but both sets

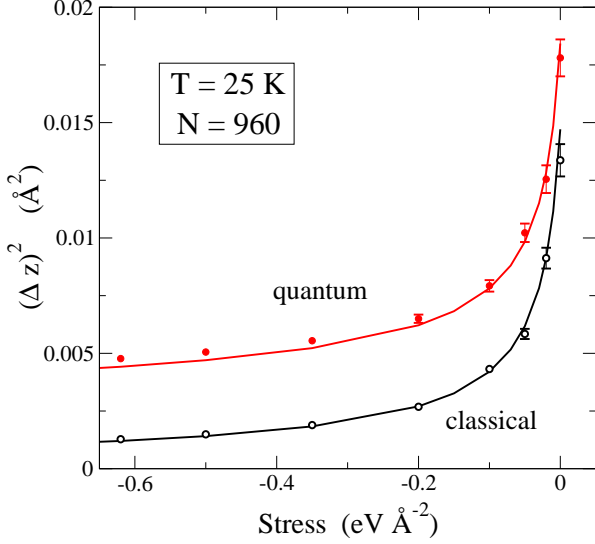


FIG. 8: Mean-square displacement in the z direction as a function of tensile stress, as derived from PIMD (solid circles) and classical (open circles) simulations for $N = 960$ and $T = 25$ K. Error bars, when not shown, are in the order or less than the symbol size. Lines were obtained from classical and quantum harmonic approximations based on ZA and ZO vibrational modes.

of results depart progressively one from the other as temperature is raised. For $P = 0$, $(\Delta z)_{\text{HA}}^2 < (\Delta z)_{\text{PI}}^2$, but the opposite happens for $T > 100$ K. For relatively large tensile stresses of -0.2 and -0.5 eV/Å⁻², we find $(\Delta z)_{\text{HA}}^2 < (\Delta z)_{\text{PI}}^2$ in the whole temperature range presented in Fig. 6. For $T > 300$ K, the difference between $(\Delta z)_{\text{PI}}^2$ and $(\Delta z)_{\text{HA}}^2$ steadily increases.

In Fig. 7 we display the mean-square displacements $(\Delta z)^2$ for $N = 960$ as a function of applied stress P for three temperatures: 100, 300, and 500 K. Symbols are results of PIMD simulations, whereas the lines correspond to the HA based on ZA and ZO vibrational modes. One observes first an important decrease in $(\Delta z)^2$ as the tensile stress is raised. This decrease is most appreciable for stresses in the range from 0 to -0.1 eV Å⁻². For larger stresses, the reduction of $(\Delta z)^2$ becomes slower. One also notices that the largest difference between $(\Delta z)_{\text{PI}}^2$ and $(\Delta z)_{\text{HA}}^2$ occurs for $P = 0$, and it becomes smaller for larger pressure. For $P \sim -0.2$ eV Å⁻², both sets of results cross each other and the data derived from PIMD become slightly larger than those corresponding to the HA.

To get better insight into the influence of nuclear quantum effects on $(\Delta z)^2$ for different pressures, we have plotted in Fig. 8 the mean-square displacements as derived from classical MD (open circles) and PIMD (solid circles) simulations at 25 K. The lines were obtained from the HA described above for the quantum case [see Eq. (14)], and

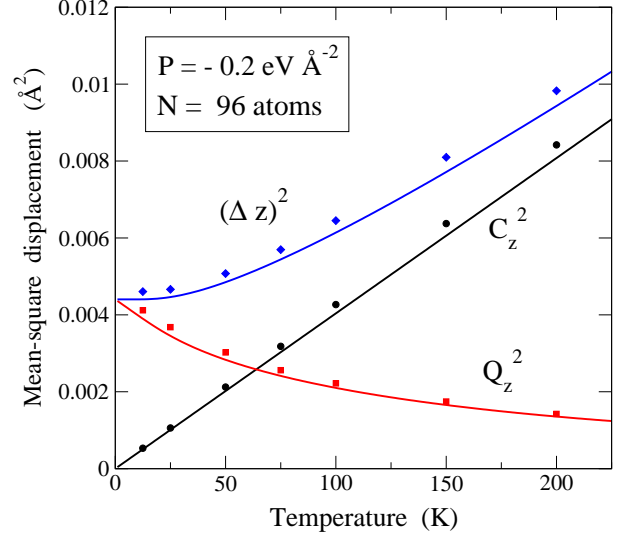


FIG. 9: Temperature dependence of the mean-square displacement along the out-of-plane direction, $(\Delta z)^2$ (diamonds), along with its classical C_z^2 (circles) and quantum Q_z^2 (squares) contributions. These data correspond to PIMD simulations for a graphene cell containing 96 atoms and a tensile stress $P = -0.2$ eV Å⁻². Lines were obtained from a harmonic approximation based on ZA and ZO vibrational modes.

for the classical calculation we used the expression

$$C_{z,\text{HA}}^2 = \frac{1}{N} \sum_{i,\mathbf{k}} \frac{k_B T}{m\omega_i(\mathbf{k})^2}. \quad (16)$$

One sees that the relevance of quantum effects increases for rising tensile stress, as can be measured from the ratio $(\Delta z)^2/C_z^2$ between the mean-square displacements in the quantum and classical case. In fact, this ratio goes from 1.3 for $P = 0$ to 3.7 for $P = -0.6$ eV Å⁻². For a given stress, the difference between the quantum results for $(\Delta z)^2$ and the classical ones, C_z^2 , decreases as temperature is raised. In fact, at $T = 300$ K the mean-square displacement derived from PIMD simulations is about 10% larger than the classical result in the stress range displayed in Fig. 8.

As indicated above, the mean-square displacement $(\Delta z)^2$ can be divided into two parts, Q_z^2 and C_z^2 , the first one properly quantum in nature, measuring the extension of the quantum paths, and the second of a classical-like character, taking account of the centroid motion, i.e., global displacements of the paths. For the sake of comparing with the results of PIMD simulations, we have also calculated in the harmonic approximation $Q_{z,\text{HA}}^2 = (\Delta z)_{\text{HA}}^2 - C_{z,\text{HA}}^2$, using Eqs. (14) and (16). To visualize the evolution of both terms as a function of temperature, we have plotted in Fig. 9 $(\Delta z)^2$ along with its two contributions Q_z^2 and C_z^2 for $N = 96$ and a stress $P = -0.2$ eV Å⁻². In the limit $T \rightarrow 0$, C_z^2 vanishes and Q_z^2 converges to a value of about 4.5×10^{-3} Å². Q_z^2 decreases for increasing temperature, as nuclear quantum

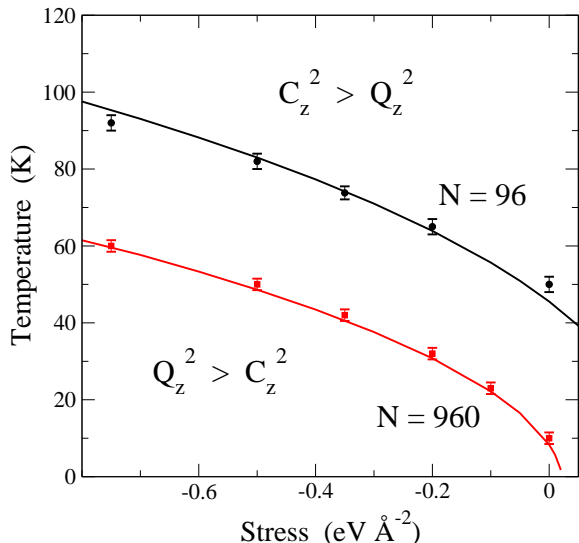


FIG. 10: $P-T$ plane displaying the crossover from the region dominated by quantum delocalization ($Q_z^2 > C_z^2$, below the lines) to the region dominated by classical-like motion ($C_z^2 > Q_z^2$, above the lines). Data points were obtained from PIMD simulations for two system sizes: $N = 96$ (circles) and 960 (squares). The lines were obtained from the HA discussed in the text.

effects become less relevant. On the contrary, the classical contribution C_z^2 increases with T , linearly in the HA [see Eq. (16)], and almost linearly for the results of PIMD simulations.

For the system size shown in Fig. 9 ($N = 96$), both contributions to $(\Delta z)^2$ are equal at $T \approx 64$ K. At higher temperatures, the classical-like part C_z^2 is the main contribution to the atomic displacements in the z direction. Values of C_z^2 given by PIMD simulations coincide within error bars with the mean-square atomic displacement obtained from classical MD simulations. The actual quantum delocalization can be estimated from the mean extension of the quantum paths in the z direction, i.e., from Q_z^2 . For $P = -0.2$ eV \AA^{-2} , we find at 25 and 300 K an average extension $(\Delta z)_Q = (Q_z^2)^{1/2} \approx 0.06$ and 0.03 \AA , respectively.

The picture displayed in Fig. 9 for the atom displacements in the out-of-plane direction is qualitatively the same for different system sizes and applied stresses, but the temperature region where Q_z^2 or C_z^2 is the main contribution to $(\Delta z)^2$ as well as the crossing point $Q_z^2 = C_z^2$ greatly depend on both variables N and P . The dependence on N is mainly caused by the enhancement of the classical-like contribution C_z^2 for increasing size, as observed earlier for results of classical MD simulations.^{37,38,46} The quantum contribution Q_z^2 has a small size effect and converges fast as N is increased.¹¹ For a given system size N , the ratio Q_z^2/C_z^2 decreases for increasing T (see Fig. 9), and there is a crossover temperature $T_c(P)$ for which this ratio is unity. For $T > T_c(P)$ classical-like motion dominates the atomic motion in the

z direction.

In Fig. 10 we present T_c as a function of the applied stress P for two system sizes: $N = 96$ and 960 . Symbols are results derived from PIMD simulations and lines correspond to crossover temperatures derived from the HA based on the ZA and ZO phonon bands. Below the lines we have $Q_z^2 > C_z^2$, i.e. the quantum contribution dominates in $(\Delta z)^2$, and the opposite happens above the lines with classical-like motion dominating the out-of-plane displacements. The crossover temperature T_c depends on the system size N , since the effective low-energy cutoff scales as $k_0 \sim N^{-1/2}$. This means that for a given stress P , an increase in N causes the appearance of ZA modes with lower frequencies, which contribute to reduce T_c (for a given ω , the classical behavior dominates for $T \gtrsim \hbar\omega/k_B$).

The main limitations of the HA are the neglect of anharmonicity in the transverse vibrational modes, which is expected to be reasonably small at low T , and the use of Eq. (15) for ZA mode frequencies under stress. This equation, giving $\omega_{\text{ZA}}(\mathbf{k})^2$ as a sum of a zero-stress term, $\omega_{\text{ZA}}^0(\mathbf{k})^2$, and a term linear in the applied stress, Pk^2/ρ , is expected to be valid for small- k ZA modes, which dominate the mean-square displacement of C atoms in the transverse direction to the graphene plane. Taking into account these limitations, the harmonic model captures qualitatively, and almost quantitatively, the basic aspects of the competition between classical-like and quantum dynamics of the C atoms in the z direction.

VI. SUMMARY

We have presented results of PIMD simulations of a graphene monolayer at several temperatures and tensile stresses. The importance of quantum effects has been quantified by comparing results of such quantum simulations with those obtained from classical MD simulations. Structural variables are found to change when quantum nuclear motion is taken into account, especially at low temperatures. Thus, the sheet area and interatomic distances change appreciably in the range of temperatures and stresses considered here.

The LCBOPII potential model was shown earlier to give a reliable description of structural and thermodynamic properties of graphene. We have investigated here its reliability to describe nuclear quantum effects in the presence of a tensile stress. The results obtained in the simulations have allowed us to analyze both the in-plane A_p and real area A of graphene as functions of T and P . The difference $A - A_p$ grows (decreases) as temperature (stress) is raised. The thermal contraction of A_p becomes less important as the tensile stress increases and the amplitude of out-of-plane vibrations decreases. We emphasize that PIMD simulations yield a negative thermal expansion of A_p at low T for pressures so high as -0.5 eV \AA^{-2} (-8 N/m). On the contrary, in classical calculations this thermal expansion becomes positive at

much smaller stresses.

Zero-point expansion of the graphene layer due to nuclear quantum effects is not negligible, and it amounts to an increase of about 1% in the area A . This zero-point effect is reduced for rising tensile stress. Moreover, the temperature dependence of the in-plane area A_p is qualitatively different when derived from PIMD or classical simulations, even at temperatures between 300 and 1000 K. Such a difference appears for all tension stresses considered here, up to $P = -0.5 \text{ eV \AA}^{-2}$.

Atomic vibrations in the out-of-plane z direction have been particularly considered, as they are important for the area A_p and for the relative stability of the planar graphene layer vs. crumpling. Quantum effects are dominant for these vibrational modes provided that $k_B T < \hbar\omega$. However, the actual atomic motion at any finite temperature, resulting from the sum of mode contributions, is dominated by the classical thermal contribution as soon as the system size is large enough. This size effect appears in the quantum simulations at low temperatures, as a result of the presence of vibrational modes in the ZA band with smaller wavenumbers (frequencies) for larger graphene cells. In this respect, an interesting result is that the temperature region where quantum motion is dominant is enhanced by an external tensile stress, as shown in Fig. 10, i.e., for a given system size T_c increases as the stress is raised.

An important point related to the consistency of the simulation results is their agreement with the principles of thermodynamics, in particular with the third law. This means that thermal expansion coefficients should converge to zero for $T \rightarrow 0$. We have found that this requirement is verified by both the in-plane area A_p and the real area A obtained from PIMD simulations for $P = 0$ and $P < 0$ (tensile stress).

An analysis of graphene under tensile stresses larger than those considered here may be interesting for its effect on mechanical, electronic, and optical properties. Such a study can be hindered by limitations associated

to effective potentials at large strains, and would require the use of *ab-initio* methods (e.g., density-functional theory). An efficient combination of these methods with path-integral simulations is still restricted to cell sizes relatively small, a limitation that is expected to be progressively overcome in the forthcoming years.

Acknowledgments

The authors acknowledge the support of J. H. Los in the implementation of the LCBOPII potential. This work was supported by Direcci3n General de Investigaci3n, MINECO (Spain) through Grants FIS2012-31713 and FIS2015-64222-C2.

Appendix A: Pressure estimator

The Cartesian coordinates of the N atomic nuclei in the crystalline membrane are denoted as \mathbf{r}_{ij} , where the $i = 1, \dots, N$ indicates the atom, and $j = 1, \dots, N_{\text{Tr}}$ refers to the bead number. The staging coordinates \mathbf{u}_{ij} are defined by a linear transformation of \mathbf{r}_{ij} that diagonalizes the *harmonic* energy associated to the effective interactions between neighboring beads:^{63,65}

$$\mathbf{u}_{i1} = \mathbf{r}_{i1} , \quad (\text{A1})$$

$$\mathbf{u}_{ij} = \mathbf{r}_{ij} - \frac{j-1}{j} \mathbf{r}_{i,j+1} - \frac{1}{j} \mathbf{r}_{i1} , \quad j = 2, \dots, N_{\text{Tr}} . \quad (\text{A2})$$

The estimator of the 2D stress tensor τ is similar to that employed in previous work for 3D systems.^{50,70} For PIMD simulations, its components are given by expressions such as⁶³

$$\tau_{xy} = \left\langle \frac{1}{A_p} \left(\sum_{i=1}^N \sum_{j=1}^{N_{\text{Tr}}} (m_j v_{ij,x} v_{ij,y} - 2k_j u_{ij,x} u_{ij,y}) - \frac{1}{N_{\text{Tr}}} \sum_{j=1}^{N_{\text{Tr}}} \frac{\partial U(\mathbf{r}_{1j}, \dots, \mathbf{r}_{Nj})}{\partial \epsilon_{xy}} \right) \right\rangle , \quad (\text{A3})$$

where the brackets $\langle \dots \rangle$ indicate an ensemble average, m_j is the dynamic mass associated to the staging coordinate \mathbf{u}_{ij} , $v_{ij,x}$, $v_{ij,y}$ are components of its corresponding velocity, and ϵ_{xy} is an element of the 2D strain tensor. The masses m_j are given by^{50,63,65}

$$m_1 = m , \quad (\text{A4})$$

$$m_j = \frac{j}{j-1} m , \quad j = 2, \dots, N_{\text{Tr}} , \quad (\text{A5})$$

where m is the nuclear mass. The constant k_j is given for each bead j by $k_j = m_j N_{\text{Tr}} / 2\beta^2 \hbar^2$ for $j > 1$ and $k_1 = 0$ ($\beta = (k_B T)^{-1}$).

The stress P used in our PIMD simulations is

$$P = \frac{1}{2} (\tau_{xx} + \tau_{yy}) , \quad (\text{A6})$$

or $P = \langle \mathcal{P} \rangle$ with the estimator

$$\mathcal{P} = \frac{1}{2A_p} \sum_{i=1}^N \sum_{j=1}^{N_{\text{Tr}}} m_j (v_{ij,x}^2 + v_{ij,y}^2) - \frac{E_h}{A_p} - \frac{1}{N_{\text{Tr}}} \sum_{j=1}^{N_{\text{Tr}}} \frac{\partial U(\mathbf{r}_{1j}, \dots, \mathbf{r}_{Nj})}{\partial A_p}. \quad (\text{A7})$$

E_h is the in-plane *harmonic* energy, that in terms of stag-

ing coordinates can be written as

$$E_h = \sum_{i=1}^N \sum_{j=2}^{N_{\text{Tr}}} k_j (u_{ij,x}^2 + u_{ij,y}^2). \quad (\text{A8})$$

The last term in Eq. (A7) is a sum of derivatives of the potential energy U at different imaginary times (beads) j . In the present case of graphene, these derivatives were carried out analytically.

-
- ¹ A. K. Geim and K. S. Novoselov, *Nature Mater.* **6**, 183 (2007).
- ² A. H. Castro Neto, F. Guinea, N. M. R. Peres, K. S. Novoselov, and A. K. Geim, *Rev. Mod. Phys.* **81**, 109 (2009).
- ³ G. W. Flynn, *J. Chem. Phys.* **135**, 050901 (2011).
- ⁴ R. Roldan, L. Chirrolli, E. Prada, J. Angel Silva-Guillen, P. San-Jose, and F. Guinea, *Chem. Soc. Rev.* **46**, 4387 (2017).
- ⁵ S. Ghosh, I. Calizo, D. Teweldebrhan, E. P. Pokatilov, D. L. Nika, A. A. Balandin, W. Bao, F. Miao, and C. N. Lau, *Appl. Phys. Lett.* **92**, 151911 (2008).
- ⁶ D. L. Nika, E. P. Pokatilov, A. S. Askerov, and A. A. Balandin, *Phys. Rev. B* **79**, 155413 (2009).
- ⁷ A. A. Balandin, *Nature Mater.* **10**, 569 (2011).
- ⁸ C. Lee, X. Wei, J. W. Kysar, and J. Hone, *Science* **321**, 385 (2008).
- ⁹ J. H. Seol, I. Jo, A. L. Moore, L. Lindsay, Z. H. Aitken, M. T. Pettes, X. Li, Z. Yao, R. Huang, D. Broido, et al., *Science* **328**, 213 (2010).
- ¹⁰ R. Prasher, *Science* **328**, 185 (2010).
- ¹¹ C. P. Herrero and R. Ramírez, *J. Chem. Phys.* **145**, 224701 (2016).
- ¹² A. Fasolino, J. H. Los, and M. I. Katsnelson, *Nature Mater.* **6**, 858 (2007).
- ¹³ J. C. Meyer, A. K. Geim, M. I. Katsnelson, K. S. Novoselov, T. J. Booth, and S. Roth, *Nature* **446**, 60 (2007).
- ¹⁴ P. L. de Andres, F. Guinea, and M. I. Katsnelson, *Phys. Rev. B* **86**, 144103 (2012).
- ¹⁵ E. Evans and W. Rawicz, *Phys. Rev. Lett.* **64**, 2094 (1990).
- ¹⁶ S. A. Safran, *Statistical Thermodynamics of Surfaces, Interfaces, and Membranes* (Addison Wesley, New York, 1994).
- ¹⁷ E. Cerda and L. Mahadevan, *Phys. Rev. Lett.* **90**, 074302 (2003).
- ¹⁸ Y. W. Wong and S. Pellegrino, *J. Mech. Materials Struct.* **1**, 3 (2006).
- ¹⁹ D. A. Kirilenko, A. T. Dideykin, and G. Van Tendeloo, *Phys. Rev. B* **84**, 235417 (2011).
- ²⁰ R. J. T. Nicholl, H. J. Conley, N. V. Lavrik, I. Vlassiuk, Y. S. Puzyrev, V. P. Sreenivas, S. T. Pantelides, and K. I. Bolotin, *Nature Commun.* **6**, 8789 (2015).
- ²¹ C. S. Ruiz-Vargas, H. L. Zhuang, P. Y. Huang, A. M. van der Zande, S. Garg, P. L. McEuen, D. A. Muller, R. G. Hennig, and J. Park, *Nano Lett.* **11**, 2259 (2011).
- ²² A. Kosmrlj and D. R. Nelson, *Phys. Rev. E* **88**, 012136 (2013).
- ²³ A. Kosmrlj and D. R. Nelson, *Phys. Rev. E* **89**, 022126 (2014).
- ²⁴ R. Ramírez and C. P. Herrero, *Phys. Rev. B* **95**, 045423 (2017).
- ²⁵ G. López-Polín, M. Jaafar, F. Guinea, R. Roldán, C. Gómez-Navarro, and J. Gómez-Herrero, *Carbon* **124**, 42 (2017).
- ²⁶ M. Pozzo, D. Alfè, P. Lacovig, P. Hofmann, S. Lizzit, and A. Baraldi, *Phys. Rev. Lett.* **106**, 135501 (2011).
- ²⁷ C. R. Woods, L. Britnell, A. Eckmann, R. S. Ma, J. C. Lu, H. M. Guo, X. Lin, G. L. Yu, Y. Cao, R. V. Gorbachev, et al., *Nature Phys.* **10**, 451 (2014).
- ²⁸ B. Amorim, A. Cortijo, F. de Juan, A. G. Grushine, F. Guinea, A. Gutierrez-Rubio, H. Ochoa, V. Parente, R. Roldan, P. San-Jose, et al., *Phys. Rep.* **617**, 1 (2016).
- ²⁹ F. Shimojo, R. K. Kalia, A. Nakano, and P. Vashishta, *Phys. Rev. B* **77**, 085103 (2008).
- ³⁰ P. L. de Andres, F. Guinea, and M. I. Katsnelson, *Phys. Rev. B* **86**, 245409 (2012).
- ³¹ G. M. Chechin, S. V. Dmitriev, I. P. Lobzenko, and D. S. Ryabov, *Phys. Rev. B* **90**, 045432 (2014).
- ³² C. P. Herrero and R. Ramírez, *Phys. Rev. B* **79**, 115429 (2009).
- ³³ E. Cadelano, P. L. Palla, S. Giordano, and L. Colombo, *Phys. Rev. Lett.* **102**, 235502 (2009).
- ³⁴ E. Akatyeva and T. Dumitrica, *J. Chem. Phys.* **137**, 234702 (2012).
- ³⁵ G.-D. Lee, E. Yoon, N.-M. Hwang, C.-Z. Wang, and K.-M. Ho, *Appl. Phys. Lett.* **102**, 021603 (2013).
- ³⁶ H.-S. Shen, Y.-M. Xu, and C.-L. Zhang, *Appl. Phys. Lett.* **102**, 131905 (2013).
- ³⁷ J. H. Los, M. I. Katsnelson, O. V. Yazyev, K. V. Zakharchenko, and A. Fasolino, *Phys. Rev. B* **80**, 121405 (2009).
- ³⁸ R. Ramírez, E. Chacón, and C. P. Herrero, *Phys. Rev. B* **93**, 235419 (2016).
- ³⁹ Y. Magnin, G. D. Foerster, F. Rabilloud, F. Calvo, A. Zappelli, and C. Bichara, *J. Phys.: Condens. Matter* **26**, 185401 (2014).
- ⁴⁰ J. H. Los, A. Fasolino, and M. I. Katsnelson, *Phys. Rev. Lett.* **116**, 015901 (2016).
- ⁴¹ M. J. Gillan, *Phil. Mag. A* **58**, 257 (1988).
- ⁴² D. M. Ceperley, *Rev. Mod. Phys.* **67**, 279 (1995).
- ⁴³ B. G. A. Brito, L. Cândido, G.-Q. Hai, and F. M. Peeters, *Phys. Rev. B* **92**, 195416 (2015).
- ⁴⁴ N. Mounet and N. Marzari, *Phys. Rev. B* **71**, 205214 (2005).
- ⁴⁵ T. Shao, B. Wen, R. Melnik, S. Yao, Y. Kawazoe, and Y. Tian, *J. Chem. Phys.* **137**, 194901 (2012).
- ⁴⁶ W. Gao and R. Huang, *J. Mech. Phys. Solids* **66**, 42 (2014).

- ⁴⁷ R. P. Feynman, *Statistical Mechanics* (Addison-Wesley, New York, 1972).
- ⁴⁸ H. Kleinert, *Path Integrals in Quantum Mechanics, Statistics and Polymer Physics* (World Scientific, Singapore, 1990).
- ⁴⁹ D. Chandler and P. G. Wolynes, *J. Chem. Phys.* **74**, 4078 (1981).
- ⁵⁰ C. P. Herrero and R. Ramírez, *J. Phys.: Condens. Matter* **26**, 233201 (2014).
- ⁵¹ J. H. Los, L. M. Ghiringhelli, E. J. Meijer, and A. Fasolino, *Phys. Rev. B* **72**, 214102 (2005).
- ⁵² L. M. Ghiringhelli, J. H. Los, A. Fasolino, and E. J. Meijer, *Phys. Rev. B* **72**, 214103 (2005).
- ⁵³ K. V. Zakharchenko, M. I. Katsnelson, and A. Fasolino, *Phys. Rev. Lett.* **102**, 046808 (2009).
- ⁵⁴ L. M. Ghiringhelli, J. H. Los, E. J. Meijer, A. Fasolino, and D. Frenkel, *Phys. Rev. Lett.* **94**, 145701 (2005).
- ⁵⁵ A. Politano, A. R. Marino, D. Campi, D. Farías, R. Miranda, and G. Chiarello, *Carbon* **50**, 4903 (2012).
- ⁵⁶ P. Lambin, *Appl. Sci.* **4**, 282 (2014).
- ⁵⁷ D. Sfyris, E. N. Koukaras, N. Pugno, and C. Galiotis, *J. Appl. Phys.* **118**, 075301 (2015).
- ⁵⁸ F. Memarian, A. Fereidoon, and M. D. Ganji, *Superlattices Microstruct.* **85**, 348 (2015).
- ⁵⁹ J.-H. Zou, Z.-Q. Ye, and B.-Y. Cao, *J. Chem. Phys.* **145**, 134705 (2016).
- ⁶⁰ A. A. Anastasi, K. Ritos, G. Cassar, and M. K. Borg, *Mol. Simul.* **42**, 1502 (2016).
- ⁶¹ H. Ghasemi and A. Rajabpour, *J. Phys. Conf. Series* **785**, 012006 (2017).
- ⁶² M. E. Tuckerman, B. J. Berne, and G. J. Martyna, *J. Chem. Phys.* **97**, 1990 (1992).
- ⁶³ M. E. Tuckerman and A. Hughes, in *Classical and Quantum Dynamics in Condensed Phase Simulations*, edited by B. J. Berne, G. Ciccotti, and D. F. Coker (World Scientific, Singapore, 1998), p. 311.
- ⁶⁴ G. J. Martyna, A. Hughes, and M. E. Tuckerman, *J. Chem. Phys.* **110**, 3275 (1999).
- ⁶⁵ M. E. Tuckerman, in *Quantum Simulations of Complex Many-Body Systems: From Theory to Algorithms*, edited by J. Grotendorst, D. Marx, and A. Muramatsu (NIC, FZ Jülich, 2002), p. 269.
- ⁶⁶ M. F. Herman, E. J. Bruskin, and B. J. Berne, *J. Chem. Phys.* **76**, 5150 (1982).
- ⁶⁷ C. P. Herrero, R. Ramírez, and E. R. Hernández, *Phys. Rev. B* **73**, 245211 (2006).
- ⁶⁸ C. P. Herrero and R. Ramírez, *J. Chem. Phys.* **134**, 094510 (2011).
- ⁶⁹ R. Ramírez, N. Neuerburg, M. V. Fernández-Serra, and C. P. Herrero, *J. Chem. Phys.* **137**, 044502 (2012).
- ⁷⁰ R. Ramírez, C. P. Herrero, E. R. Hernández, and M. Cardona, *Phys. Rev. B* **77**, 045210 (2008).
- ⁷¹ J.-B. Fournier and C. Barbetta, *Phys. Rev. Lett.* **100**, 078103 (2008).
- ⁷² A. Imparato, *J. Chem. Phys.* **124**, 154714 (2006).
- ⁷³ Q. Waheed and O. Edholm, *Biophys. J.* **97**, 2754 (2009).
- ⁷⁴ E. Chacón, P. Tarazona, and F. Bresme, *J. Chem. Phys.* **143**, 034706 (2015).
- ⁷⁵ R. J. T. Nicholl, N. V. Lavrik, I. Vlassiuk, B. R. Srijanto, and K. I. Bolotin, *Phys. Rev. Lett.* **118**, 266101 (2017).
- ⁷⁶ K. R. Hahn, C. Melis, and L. Colombo, *J. Phys. Chem. C* **120**, 3026 (2016).
- ⁷⁷ K. H. Michel, S. Costamagna, and F. M. Peeters, *Phys. Status Solidi B* **252**, 2433 (2015).
- ⁷⁸ L. D. Landau and E. M. Lifshitz, *Statistical Physics* (Pergamon, Oxford, 1980), 3rd ed.
- ⁷⁹ C. P. Herrero, *Phys. Rev. B* **65**, 014112 (2002).
- ⁸⁰ C. P. Herrero and R. Ramírez, *Phys. Rev. B* **51**, 16761 (1995).
- ⁸¹ L. D. Landau and E. M. Lifshitz, *Quantum Mechanics* (Pergamon, Oxford, 1965), 2nd ed.
- ⁸² M. J. Gillan, in *Computer Modelling of Fluids, Polymers and Solids*, edited by C. R. A. Catlow, S. C. Parker, and M. P. Allen (Kluwer, Dordrecht, 1990), p. 155.
- ⁸³ L. J. Karssemeijer and A. Fasolino, *Surf. Sci.* **605**, 1611 (2011).
- ⁸⁴ L. Wirtz and A. Rubio, *Solid State Commun.* **131**, 141 (2004).